A computational and spectroscopic study of Dy^{3+} doped $BaAl_2O_4$ phosphors

Marcos V dos S. Rezende[1*], Paulo J R Montes[2], Mário E G Valerio[3], Robert A Jackson[4]

[1] Grupo de Nanomateriais Funcionais (GNF), Departamento de Física, Universidade Federal de Sergipe, Campus Universitário, 49100-000 Itabaiana-SE, Brasil

[2]Coordenadoria de Física, Instituto Federal de Sergipe, 49400-000, Lagarto-SE, Brasil

[3] Departamento de Física, Universidade Federal de Sergipe, Campus Universitário, 49100-000 São Cristovão-SE, Brasil

[4] School of Chemical and Physical Sciences, Keele University, Keele, Staffordshire, ST5 5BG, UK

Abstract: Computational and experimental methods are employed to study the optical properties of Dy-doped $BaAl_2O_4$ matrix. Atomistic modelling is used to make predictions of Dy doping sites and charge compensation schemes. The symmetry predicts from atomistic modeling was used to calculate crystal field parameters and to obtain the energies of the electronic transitions of the Dy^{3+} ion. Dy-doped $BaAl_2O_4$ was prepared via a sol-gel proteic technique. The optical properties were studied using X-ray excited optical luminescence (XEOL) measurements. The X-ray absorption near-edge structure (XANES) at the Ba and Eu L_{III}-edges exhibits typical absorption spectra. The area under the XEOL spectra increases as the photon energy increases in the region around the Ba and Dy L_{III}-edges. The XEOL spectra showed typical Dy lines. Experimental and calculated values for the transition energies are compared.

Keywords: A. optical materials B. computer modelling and simulation; D. defects; D. optical properties; D. luminescence.

*Corresponding author: Tel.: +55 79 99932 2462
E-mail address: mvsrezende@gmail.com (M. V. dos S. Rezende)

1. Introduction

Dysprosium is a rare earth ion widely used as an activator dopant in many different materials. In general, the Dy^{3+} ions act as hole traps in the different aluminates [1] including $SrAl_2O_4$: Eu^{2+}, Dy^{3+} [2], $BaAl_2O_4$: Eu^{2+}, Dy^{3+} [3], $CaAl_2O_4$: Eu^{2+}, Dy^{3+} [4] and $Sr_4Al_{14}O_{25}$: Eu^{2+}, Dy^{3+} [5] and aluminosilicates including $Ca_2Al_2SiO_7$: Eu^{2+}, Dy^{3+}, $Sr_2Al_2SiO_7$: Eu^{2+}, Dy^{3+} [6], $CaAl_2Si_2O_8$: Eu^{2+}, Dy^{3+} [7] to increase the persistence of the luminescence. In other aluminates, and silicates including $CaAl_2O_4$: Dy^{3+} [8] and Gd_2SiO_5: Dy^{3+} [9], Dy^{3+} ions act as luminescence centres, important for solid-state laser applications.

$BaAl_2O_4$:Dy^{3+} [10] $BaAl_2O_4$: Eu^{2+}, Dy^{3+} [3] and $BaAl_2O_4$: Nd^{3+}, Dy^{3+} [11] phosphors show longer luminescence persistence as compared with sulphide phosphors [12]. These materials can be used in a wide range of applications, including luminous paints for highways, airports, buildings and ceramic products [1]. In addition, they can also be used in textiles, dial plates of luminous watches, warning signs, escape routes and other applications [13].

The duration of the persistent emission is increased by co-doping with Dy^{3+} ions. Many studies have been dedicated to understanding the relationship between Dy^{3+} ions and hole traps. However, this relationship is still not fully understood. Some studies proposed that the Dy^{3+} ion traps a hole, e.g. [14] while others proposed that the Dy^{3+} ions induce the formation of hole traps associated with a charge compensating defect, e.g. [15]. Knowing

the position and the effect of a Dy^{3+} ion on the local structure of the $BaAl_2O_4$ matrix can help clarify the trapping mechanism of carriers in the luminescence process.

Therefore, in order to understand the defect properties generated by Dy^{3+} ions in the $BaAl_2O_4$ matrix, the present study employed atomistic simulation techniques and X-ray Excited Optical Luminescence (XEOL) technique spectroscopy. The minimized energy locations of the Dy dopant ion and its surrounding ions are used to obtain crystal field parameters, based on the simple overlap model (SOM), and the crystal field parameters are in turn used to calculate the energies of the electronic transitions of the Dy ion doped into the $BaAl_2O_4$ matrix. The X-ray Excited Optical Luminescence (XEOL) technique was employed to probe the luminescence properties of Dy^{3+}-doped $BaAl_2O_4$, and the predicted electronic transitions were compared to the XEOL spectrum.

2. Modelling and Experimental Procedure

2.1 Modelling

Atomistic modelling methods have been widely used in studies of doped materials [16–20]. In these methods, the interactions between ions in the solid are described through a set of interatomic potentials. The potential parameters for $BaAl_2O_4$ were obtained by empirical fitting, as described in a previous paper [21] using the GULP code [22]. The experimental and calculated lattice parameters show an agreement of 2% or better.

Defect properties were calculated using the Mott–Littleton [23] method in which a spherical region of lattice surrounding the defect (region I) is treated explicitly, with all interactions being considered, and more distant parts of the lattice (region II) are treated

using a continuum approach. Having obtained the positions of the dopant ion, and the relaxed positions of the surrounding ions, these are input into a crystal field calculation based on the Simple Overlap model (SOM) [24]. The energies levels were calculated from the crystal field parameters obtained using relaxed positions of the dopant ions and the surrounding lattice ions are obtained from the atomistic calculations together with the free ion parameters obtained for the LaF_3 system[25] where the La^{3+} ion was substituted by each of the ions in the lanthanide series. The same procedure was used in a previous study of $Sr_3Al_2O_6:Eu^{3+}$ [17] and $BaAl_2O_4:Eu^{3+}$ phosphors [26].

2.2 Experimental procedure

$Ba_{0.97}Dy_{0.03}Al_2O_4$ samples were produced using a sol-gel proteic route [27]. In this route, the reagent was mixed with coconut water (*Cocos nucifera*) forming the starting gel and then dried at 100 °C for 24 hours, forming a xerogel. In the next step the xerogel is calcined at 1100 °C for 2 hours. More details of the procedure can be found in a previous reference [28]. The existence of a single crystalline phase was confirmed by X-ray diffraction measurements. The X-ray Absorption Spectroscopy (XAS) measurements were collected using the XAFS2 beamline at the LNLS (Brazilian Synchrotron Light Laboratory, Campinas, Brazil) around the Ba and Dy L_{III}-edge at room temperature in transmission mode. XEOL spectra were measured simultaneously with the XAS spectra using an Ocean Optics HR2000 spectrometer and an optical fibre.

3. Discussion

$BaAl_2O_4$ has a hexagonal structure with a ferroelectric phase transition at T = 396 K [29]. It belongs to the family of stuffed tridymites which are derived from the structure of SiO_2 β-tridymite. The structure has a three-dimensional network of corner-sharing AlO_4 tetrahedra, with hexagonal channels occupied by Ba^{2+} ions. There are two non-equivalent Ba^{2+} sites having different coordination numbers (8 and 9) and similar average Ba-O distances (2.85 Å and 2.87 Å). There are four non-equivalent Al^{3+} sites which have similar average Al-O distances (1.73, 1.75, 1.77 and 1.81 Å).

In principle, a Dy^{3+} ion can substitute at either an Al^{3+} or a Ba^{2+} site. The ionic radius and oxidation numbers are the two parameters which determine the localisation of the Dy^{3+} ion. The capability of $BaAl_2O_4$ to accommodate a Dy^{3+} ion is of fundamental importance for its optical properties. The influence of the Dy^{3+} ion depends on the substitution site (Al^{3+} or Ba^{2+}) as well as the defects required for charge compensation. When the Dy^{3+} ion is substituted at the Al^{3+} site, no charge compensation is needed. On the other hand, charge compensation is required when the Ba^{2+} ion is the host site. Charge compensation can occur by Ba^{2+} vacancies, anti-site defects, interstitial O^{2-} ions or Al^{3+} vacancies. In order to model the different charge compensation mechanisms, a range of reactions schemes have been developed, as shown in table 1. Scheme (i) represents substitution at the Al^{3+} site, while schemes (ii) to (v) are for reactions involving substitution at the Ba^{2+} site with a range of charge compensation mechanisms.

Table 1 – Reaction schemes for solution of rare-earth dopants.

Reactions schemes
$(i)\ 0.5Dy_2O_3 + Al_{Al} \rightarrow Dy_{Al} + 0.5Al_2O_3$
$(ii)\ Dy_2O_3 + 3Ba_{Ba} \rightarrow (2Dy_{Ba}^{\bullet} + V_{Ba}'') + 3BaO$
$(iii)\ 0.5Dy_2O_3 + Ba_{Ba} + Al_{Al} \rightarrow (Dy_{Ba}^{\bullet} + Ba_{Al}') + 0.5Al_2O_3$
$(iv)\ Dy_2O_3 + 2Ba_{Ba} \rightarrow (2Dy_{Ba}^{\bullet} + O_i'') + 2BaO$
$(v)\ 0.5Dy_2O_3 + 3Ba_{Ba} + Al_{Al} \rightarrow (3Dy_{Ba}^{\bullet} + V_{Al}''') + 3BaO + 0.5Al_2O_3$

The solution energies were calculated by combining the incorporation of Dy dopant in the host site with the appropriate defect and lattice energy terms for each reaction scheme showed in table 1. These are defined as the total energy involved in the doping process, including charge compensation if needed. Since there is more than one non-equivalent Al^{3+} or Ba^{2+} site, all the defects have more than one possible symmetry configuration and the more provable was showed in Figure 1.

The results show that the reaction scheme (iv), involving the substitution of Dy^{3+} at the Ba^{2+} site with the oxygen interstitial compensation is more energetically favourable, with a solution energy of 2.94 eV. The second most favourable defect involves the substitution of a Dy^{3+} ion at the Al^{3+} site, with solution energy of 3.08 eV. The relatively small solution energies difference between schemes (i) and (iv), 0.14 eV, indicates a possibility of a Dy^{3+} ion substituting at both cationic host sites. This can be explained in terms of the size difference between the Dy^{3+} ion and the host sites. The ionic radius of Dy^{3+} (0.912 Å) is greater than the radius of Al^{3+} (0.39 Å), and is smaller than the radius of Ba^{2+} (1.47 Å) [30]. When Dy^{3+} ions substitute at the Al^{3+} site, the relative ionic radius difference (0.522 Å) is very similar to when Dy^{3+} ions substitute at the Ba^{2+} site (0.558 Å). In both cases it is possible that large distortions are caused by the expansion or contraction of the first nearest neighbours. Schemes (ii) and (v), which involve charge compensation by a Ba^{2+} or Al^{3+}

vacancies respectively, have large solution energies due to the large deformation caused by the creation of a cationic vacancy. For scheme (iii), the large solution energy can be explained by the size difference of the Ba^{2+} and Al^{3+} ions, which causes a distortion of the oxygen tetrahedron.

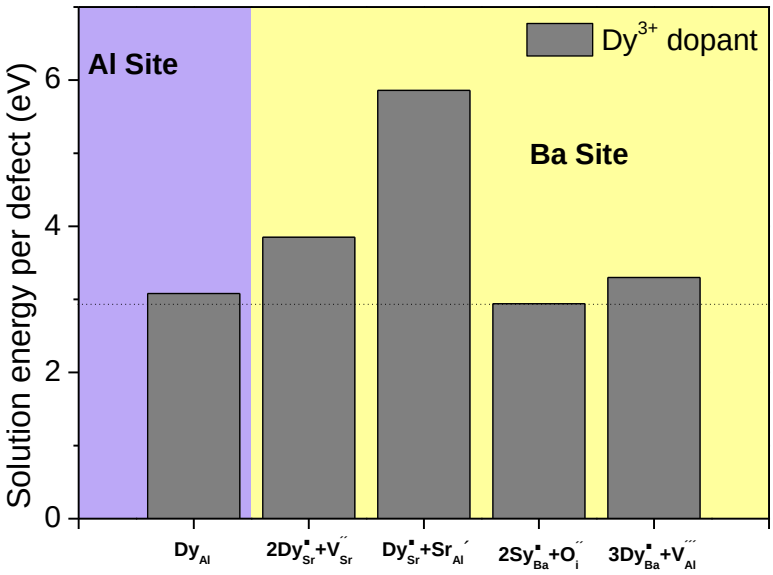

Figure 1 – Solution energy for europium ion in the $BaAl_2O_4$ structure.

The persistent luminescence mechanism of $SrAl_2O_4:Eu^{2+}$, Dy^{3+} proposed by Clabau et al. [1] can also be applied to $BaAl_2O_4:Eu^{2+}$, Dy^{3+} and it suggests that Ba^{2+} and O^{2-} vacancies act as electron traps. TL (thermoluminescence) experimental results from Beauger [31] showed that the Dy^{3+} ion increases the number and the depth of the electron traps, but from atomistic simulations it can be seen that Dy^{3+} substitution in the host site (Al^{3+} or Ba^{2+}) does not contribute to the increase in the number of Ba^{2+} or O^{2-} vacancies. The solution energies clearly show that the most stable defects are those that do not involve vacancy formation as charge compensating defects.

The defect configuration for Dy^{3+} substitution in the Ba^{2+} sites, that gives the lowest solution energy, was used to calculate the crystal field parameters (B^k_q) using the simple overlap model (SOM) [24]. The set of non-zero B^k_q components provide an unambiguous indication of the local symmetry of the central optically active ion. The relaxed positions of the dopant ions and the surrounding lattice ions are obtained. Table 2 gives the B^k_q values for the Dy^{3+} substitution at Ba site. It is noted that all parameters are non-zero, indicating that the symmetry of the substitution site is low, indicating that C_1 symmetry is probable. This due to the lattice distortion generated by ionic radii differences between the dopant and matrix sites.

Table 2 – The crystal field parameters for the Dy^{3+} substitution at Ba site.

B^k_q	Ba site	B^k_q	Ba site
B^2_0	96.2	B^6_0	-134.7
B^2_1	379.0+619.8i	B^6_1	-138.5-174.5i
B^2_2	122.8+808.5i	B^6_2	97.2-32.3i
B^4_0	-415.8	B^6_3	-355.4+87.1i
B^4_1	0.3-8.7i	B^6_4	-181.6-255.9i
B^4_2	-159.7+189.7i	B^6_5	28.7-204.4i
B^4_3	-568.1+64.4i	B^6_6	-24.7+38.9i
B^4_4	-51.4+111.8i		

Table 3 shows the energy level predicted for Dy^{3+} substituting at Ba site, using the B^k_q values from Table 2. Having determined the energy levels, it is possible to calculate all allowed transitions. As the Dy^{3+} ion exhibits low symmetry, as shown by the B^k_q values, all $^4F_{9/2} \rightarrow {}^6H_J$ (J=9/2, 11/2, 13/2, 15/2) transitions are allowed by an electric dipole mechanism. Table 4 shows all allowed transitions when the Dy^{3+} is substituted at Ba site. Forty and thirty-five emissions are observed due to the $^4F_{9/2} \rightarrow {}^6H_{15/2}$ and $^4F_{9/2} \rightarrow {}^6H_{13/2}$ transitions, respectively. The total splitting of wavelength of the $^4F_{9/2} \rightarrow {}^6H_{15/2}$ and $^4F_{9/2} \rightarrow {}^6H_{13/2}$ transitions are 31.1 and 33.8 nm, respectively. In the $^4F_{9/2} \rightarrow {}^6H_{11/2}$ and $^4F_{9/2} \rightarrow {}^6H_{9/2}$

transitions, a total of the thirty and twenty-five emissions are observed respectively. This transition shows a total splitting greater than for the $^4F_{9/2}\rightarrow{}^6H_{13/2;15/2}$ transitions. The total splitting of the $^4F_{9/2}\rightarrow{}^6H_{11/2;9/2}$ transition 35.8 and 38.1 nm. Large values of the total splitting may explain wide lines in the experimental spectrum. This information will be discussed in more detailed in the next paragraph.

Table 3 – Energy levels of Dy in $BaAl_2O_4$.

$^6H_{15/2}(cm^{-1})$	$^6H_{13/2}(cm^{-1})$	$^6H_{11/2}(cm^{-1})$	$^6H_{9/2}(cm^{-1})$	$^4F_{9/2}(cm^{-1})$
0.0	2480.7	4323.0	5721.8	19193.4
229.8	2694.3	4441.7	5799.1	19252.9
433.7	2836.8	4556.0	5911.6	19266.6
542.4	2925.8	4636.2	5997.2	19311.1
657.8	2991.7	4731.5	6188.1	19404.9
745.0	3075.1	4883.8		
788.0	3186.1			
891.4				

In Table 5 the difference between the predicted and the experimental wavelength transition of Dy^{3+} is shown. It can be seen that the agreement between the predicted and the experimental values is better than ±5% for the $^4F_{9/2}\rightarrow{}^6H_J$ (J=11/2, 13/2, 15/2) transitions, and that for the $^4F_{9/2}\rightarrow{}^6H_{9/2}$ transition, this difference is better than ±1%. The difference between the predicted average transitions is around 1 nm.

Table 4 – All possible transition of Dy^{3+} ion in $BaAl_2O_4$.

$^4F_{9/2}\rightarrow{}^6H_{15/2}$	$^4F_{9/2}\rightarrow{}^6H_{13/2}$	$^4F_{9/2}\rightarrow{}^6H_{11/2}$	$^4F_{9/2}\rightarrow{}^6H_{9/2}$
515.3	590.9	663.0	730.8
517.8	594.2	667.2	734.9
519.0	595.7	668.3	735.8
519.4	596.2	669.2	738.2
521.0	598.3	669.8	739.0
521.5	598.4	672.5	740.0
524.1	601.8	672.5	741.1
525.3	603.4	673.5	742.3
525.7	603.6	674.5	742.5
527.1	603.9	675.2	743.2
527.3	606.1	677.1	745.8
529.7	606.8	677.7	746.3
530.2	607.0	677.9	746.5
531.0	608.7	679.8	749.5
531.1	609.2	680.4	751.0
531.4	609.3	681.4	752.9
532.8	610.3	681.5	754.3
533.4	611.4	683.2	756.6
534.1	612.0	683.5	757.7
534.5	612.4	684.1	748.7
535.9	612.5	685.9	753.6
536.1	612.8	686.9	762.0
536.2	614.4	688.0	764.6
537.1	614.7	688.6	765.4
537.4	615.0	688.7	768.9
537.8	615.9	691.5	
538.6	616.6	693.1	
539.5	617.2	695.3	
539.9	617.6	695.9	
539.9	618.1	698.8	
540.1	620.2		
540.3	620.4		
541.2	621.9		
541.6	622.4		
542.1	624.7		
542.9			
543.3			
544.2			
544.6			
546.4			

Table 5 – Comparison between experimental and theoretical results of transition wavelengths of the Dy^{3+} ion in $BaAl_2O_4$.

Transitions	$^4F_{9/2}\rightarrow{}^6H_{15/2}$	$^4F_{9/2}\rightarrow{}^6H_{13/2}$	$^4F_{9/2}\rightarrow{}^6H_{11/2}$	$^4F_{9/2}\rightarrow{}^6H_{9/2}$
Experimental	512.3	577.1	662.9	752.8
Theory (Average)(Al2)	534.3	611.3	682.4	749.7
Theory(Average)(Ba2)	533.5	609.8	680.8	748.5
Difference (Theo./Exp.) (%)	-4,14	-5.66	-2.70	0.57

Figure 2 and 3 show the area of XEOL curves as a function of X-ray energy when the sample of $BaAl_2O_4$:Dy^{3+} is excited around Ba L_{III}-edge and Dy L_{III}-edge, respectively. At the absorption edge, the attenuation length of X-ray photons in the material abruptly increases as observed in the XANES spectra. The area under the XEOL spectra increases as the photon energy increases and with a well-pronounced edge jump at ~ 5247 eV (Ba L_{III}-edge) and at ~7790 eV (Dy L_{III}-edge). This means that the intensity of luminescence depends on the excitation energy. This behaviour can be explained in terms of secondary de-excitation processes. This result can also be interpreted in terms of the model described in a previous paper [32]. When the sample is excited at the Ba L_{III}-edge, secondary de-excitation processes like X-ray fluorescence emission occur with principal X-ray fluorescence lines due to the Ba $L_{\alpha1}$ (4466.5 eV) and $L_{\beta2}$ (5154.4 eV) transitions. These energies, however, are not efficiently absorbed by other ions of the crystalline matrix (i.e. Al^{3+} and O^{2-}) since these energies are far from the more energetic K absorption lines of Al and O at 1559 eV and 543.1 eV (K-edge), respectively. The dopant also does not efficiently absorb these photons since the closest absorption line of the Dy ion is the $L_{I\text{-}III}$-edge, around 9046-7790 eV, or the $M_{I\text{-}V}$-edge, around 2047-1292 eV. When the sample is excited at the Dy L_{III}-edge the main X-ray fluorescence emission lines from the secondary de-excitation processes occur via Dy $L_{\alpha1}$ (6498 eV) and $L_{\beta2}$ (7636.4 eV). These values are far from any absorption lines due to ions in

the crystalline matrix. Therefore, these secondary de-excitation processes do not cause a decrease in electron-hole pair creation and, consequently, do not cause a decrease of Dy^{3+} ion luminescence.

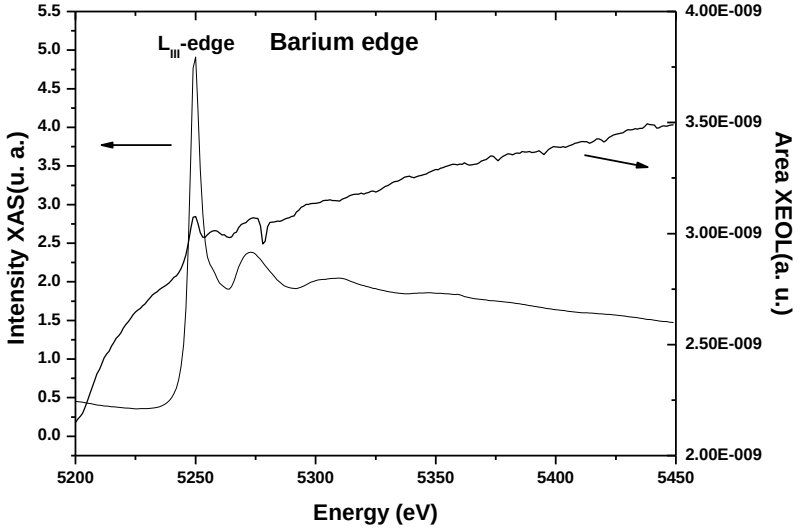

Figure 2 – XAS and XEOL curves of $BaAl_2O_4:Dy^{3+}$ excited in the region of Ba L_{III}-edges.

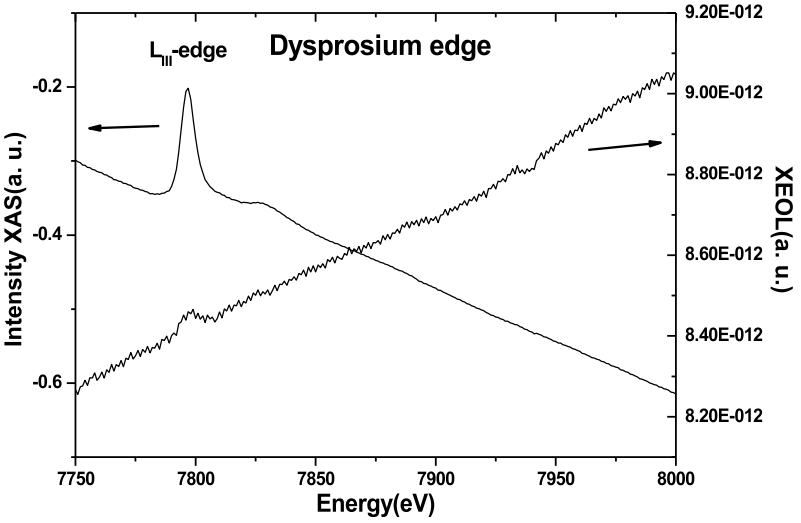

Figure 3 – XAS and XEOL curves of $BaAl_2O_4:Dy^{3+}$ excited in the region of Dy L_{III}-edges.

XEOL spectra excited at energies near the Ba and Dy L_{III}-edge are shown in Fig. 4 and 5, respectively. In both case, the emission intensity of Dy^{3+} increases with an increase of the excitation energy. The spectra have four sharp peaks, the characteristic emission lines from Dy^{3+} ions. The two first peaks at 512.3 nm and 577.1 nm correspond to $^4F_{9/2}\rightarrow{}^6H_{15/2}$ and $^4F_{9/2}\rightarrow{}^6H_{13/2}$ transitions respectively. The $^4F_{9/2}\rightarrow{}^6H_{15/2}$ transition is mainly magnetically allowed and hardly varies with the crystal field strength around the dysprosium ion [33,34]. On the other hand, the $^4F_{9/2}\rightarrow{}^6H_{13/2}$ transition is a forced electric dipole transition that is sensitive to the coordination environment. When the Dy^{3+} ion is located at a low-symmetry local site (without an inversion centre), this emission has been prominent in the emission spectrum (hypersensitive transition). Therefore, the Dy^{3+} ions are occupying low symmetry sites since the electric dipole $^4F_{9/2}\rightarrow{}^6H_{13/2}$ transitions are stronger than that of the magnetic-dipole $^4F_{9/2}\rightarrow{}^6H_{15/2}$ transition in Figs. 4-5. This conclusion is agreement with the crystal field parameters values obtained from atomistic simulation. The second two peaks at 662.9 nm and 752.8 nm correspond to $^4F_{9/2}\rightarrow{}^6H_{11/2}$ and $^4F_{9/2}\rightarrow{}^6H_{9/2}$ transitions of the Dy^{3+} ion, respectively. In general, the emission lines of the rare earth ions are close due the screening effect of the d layer, but in the emission spectrum a broad band is observed. This is due to the large splitting of the possible transition attributed to each one of the $^4F_{9/2}\rightarrow{}^6H_J$ (J=11/2, 13/2, 15/2) transitions. From atomistic calculations, it can be seen that the total splittings for the $^4F_{9/2}\rightarrow{}^6H_{15/2}$ and $^4F_{9/2}\rightarrow{}^6H_{13/2}$ transitions are about 31.6 and 33.8 nm, respectively, and for the $^4F_{9/2}\rightarrow{}^6H_{11/2}$ and $^4F_{9/2}\rightarrow{}^6H_{9/2}$ transitions they are about 37.9 and 45.1 nm, respectively.

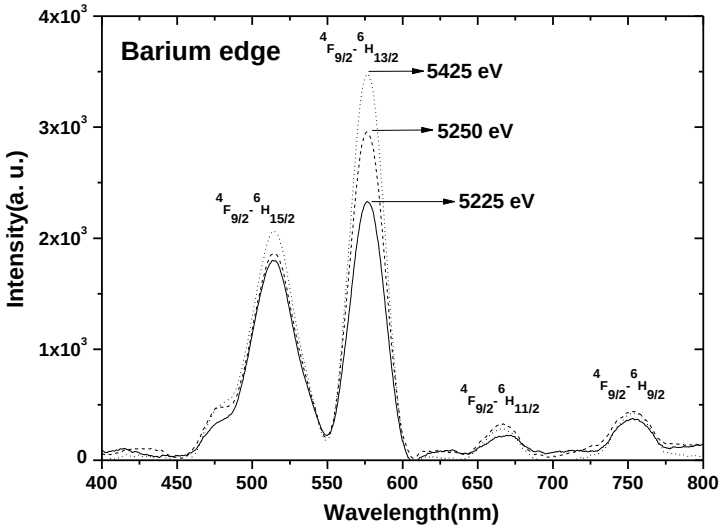

Figure 4 – Spectrum XEOL excited at Ba L_{III}-edge.

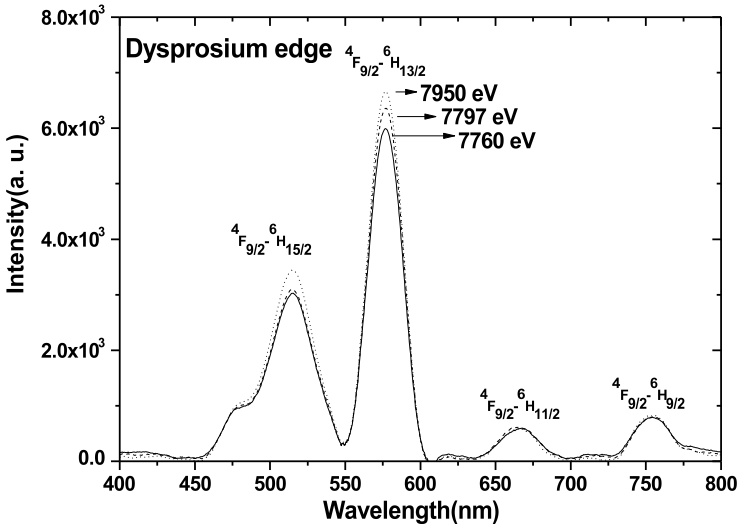

Figure 5 – Spectrum XEOL excited at Ba L3-edge and Eu L3-edge.

The emission spectrum of of Dy-doped $BaAl_2O_4$ is not reported in the literature, but Dy doped in other aluminates like $SrAl_2O_4$ and $CaAl_2O_4$ is found or reported. The intense peak observed at 577.1 nm is in agreement with the 577 nm peak observed in the photoluminescence spectrum of $CaAl_2O_4$: Dy^{3+} reported by Liu et al. [8], and close to 570 nm

observed in the radioluminescence spectrum of $SrAl_2O_4:Eu^{2+}$, Dy^{3+} reported by Montes et al. [35]. A less intense peak at 662.9 nm, attributed to the $^4F_{9/2} \rightarrow {}^6H_{11/2}$ transition, is close to the 668 nm peak reported by Liu et al. [8]. The small difference found in the wavelength of emission between the other experimental papers and this paper is due the difference in symmetry of host sites in the different aluminates. Several authors [36,37] observed the typical transition of the Dy in other host materials.

Figure 6 shows the XEOL spectrum when the sample is excited with X-ray photons at the Ba L_{III}-edge (5225 eV) and Dy L_{III}-edge (7797 eV) and the theoretical transition lines. The spectra show more intense luminescence when the sample is excited at the Dy L_{III}-edge than the Ba L_{III}-edge. This result reveals that the greater the excitation energy the greater the intensity of the emission spectrum. This effect can be related to the number of electron-hole pairs created extended by increase in the excitation energy, following the mechanism of XEOL in $BaAl_2O_4$:Ce proposed in the previous paper [32].

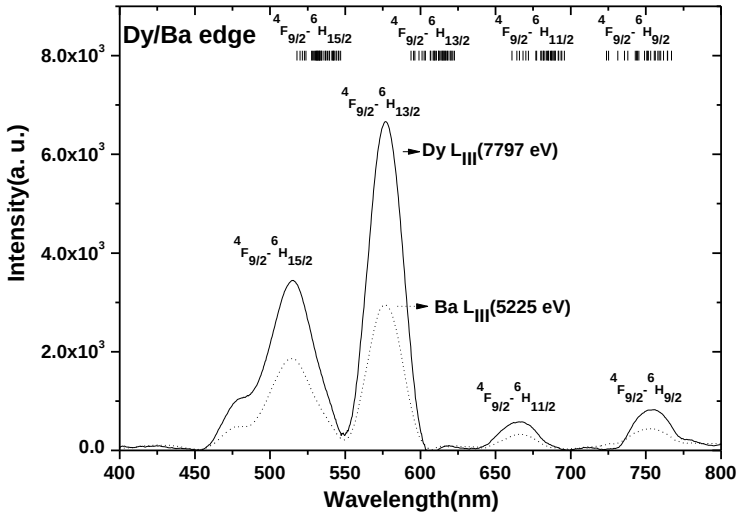

Figure 6 – Spectrum XEOL excited at Ba L_{III}-edge and Dy L_{III}-edge.

4. Conclusion

The location of the Dy^{3+} ion in $BaAl_2O_4$ has been investigated by the atomistic simulation. The results show that the substitution of Dy^{3+} at the Ba^{2+} site with the oxygen interstitial compensation is more energetically favourable. The intensity of XEOL spectrum increases as the energy of the photons increases when the sample is excited at Ba L_{III}-edge and Dy L_{III}-edge. The transition energy calculated by the hybrid computational method and the value obtained from the XEOL spectrum are in good agreement of 5%. The XEOL spectra show an intense peak attributed to the $^4F_{9/2} \rightarrow {}^6H_{13/2}$ transition indicating the low symmetry of Dy^{3+} ion in the matrix and in agreement with the crystal field parameters obtained by computational methods.

Acknowledgments

The authors are grateful to FINEP, CAPES, CNPq (Project No. 470.972/2013-0) for financial support. Synchrotron measurements were done at the LNLS—Brazilian Synchrotron Light Laboratory/CNPEM/MCT under proposal No. XAFS2 #18003/15.

References

[1] F. Clabau, X. Rocquefelte, S. Jobic, P. Deniard, M.-H. Whangbo, A. Garcia, T. Le Mercier, Chem. Mater. 17 (2005) 3904–3912.

[2] H. Sun, L. Pan, X. Piao, Z. Sun, J. Mater. Chem. A 1 (2013) 6388.

[3] R. Sakai, T. Katsumata, S. Komuro, T. Morikawa, J. Lumin. 85 (1999) 149–154.

[4] T. Katsumata, T. Nabae, K. Sasajima, T. Matsuzawa, J. Cryst. Growth 183 (1998) 361–365.

[5] Y. Lin, Z. Tang, Z. Zhang, Mater. Lett. 51 (2001) 14–18.

[6] N. Kodama, N. Sasaki, M. Yamaga, Y. Masui, J. Lumin. 94–95 (2001) 19–22.

[7] N.Y. He, S.X. Ge, C. Yang, J.M. Cao, M. Gu, Mater. Lett. 58 (2004) 3304–3307.

[8] B. Liu, C. Shi, Z. Qi, Appl. Phys. Lett. 86 (2005) 191111.

[9] R. Lisiecki, G. Dominiak-Dzik, P. Solarz, W. Ryba-Romanowski, M. Berkowski, M. Głowacki, Appl. Phys. B 98 (2009) 337–346.

[10] B. Zhai, Q. Ma, R. Xiong, X. Li, Y.M. Huang, Mater. Res. Bull. 75 (2016) 1–6.

[11] Z. Qiu, Y. Zhou, M. Lü, A. Zhang, Q. Ma, Acta Mater. 55 (2007) 2615–2620.

[12] W. Hoogenstraaten, H.A. Klasens, J. Electrochem. Soc. 100 (1953) 366.

[13] H. Yamamoto, T. Matsuzawa, J. Lumin. 72–74 (1997) 287–289.

[14] T. Matsuzawa, J. Electrochem. Soc. 143 (1996) 2670.

[15] M. OHTA, M. MARUYAMA, T. HAYAKAWA, T. NISHIJO, J. Ceram. Soc. Japan 108 (2000) 284–289.

[16] M.V.D.S. Rezende, R.M. Araujo, M.E.G. Valerio, R. a Jackson, J. Phys. Conf. Ser. 249 (2010) 012042.

[17] M.V.S. Rezende, R.M. Araújo, P.J.R. Montes, M.E.G. Valerio, Opt. Mater. (Amst). 32 (2010) 1341–1344.

[18] M.V.D.S. Rezende, J. Phys. Chem. Solids 75 (2014) 1113–1118.

[19] R.D.S. Santos, M.V. dos S. Rezende, Adv. Condens. Matter Phys. 2014 (2014) 1–8.

[20] M.V. dos S. Rezende, J.B. Amaral, M.E.G. Valerio, R.A. Jackson, Opt. Mater. (Amst). 48 (2015) 105–109.

[21] M.V.D.S. Rezende, M.E.G. Valerio, R. a. Jackson, Opt. Mater. (Amst). 34 (2011) 109–118.

[22] J.D. Gale, J. Chem. Soc. Faraday Trans. 93 (1997) 629–637.

[23] N.F. Mott, M.J. Littleton, Trans. Faraday Soc. 34 (1938) 485.

[24] O.L. Malta, Chem. Phys. Lett. 88 (1982) 353–356.

[25] W.T. Carnall, G.L. Goodman, K. Rajnak, R.S. Rana, J. Chem. Phys. 90 (1989) 3443–3457.

[26] M.V. do. S. Rezende, P.J. Montes, M.E.G. Valerio, R.A. Jackson, Opt. Mater. (Amst). 34 (2012) 1434–1439.

[27] J.M. Macedo, M. A., Sasaki, “Processo de Fabricação de Pós Nanoparticulados”INPI 0203876-5, n.d.

[28] M.V. dos S. Rezende, C. Arrouvel, S.C. Parker, J.F.Q. Rey, M.E.G. Valerio, Mater. Chem. Phys. 136 (2012) 1052–1059.

[29] S.-Y. Huang, R. Von Der Mühll, J. Ravez, J.P. Chaminade, P. Hagenmuller, M. Couzi, J. Solid State Chem. 109 (1994) 97–105.

[30] R.D. Shannon, J. Appl. Phys. 73 (1993) 348–366.

[31] C. Beauger, Beauger, C. Thesis, Universitéde Nice, Nice, France, 1999., Universitéde Nice, France, 1999.

[32] M.V. dos S. Rezende, P.J.R. Montes, M.E.G. Valerio, J. Lumin. 132 (2012) 1106–1111.

[33] E. Cavalli, M. Bettinelli, A. Belletti, A. Speghini, J. Alloys Compd. 341 (2002) 107–110.

[34] F. Gu, S.F. Wang, M.K. Lü, W.G. Zou, G.J. Zhou, D. Xu, D.R. Yuan, J. Cryst. Growth 260 (2004) 507–510.

[35] P.J.R. Montes, M.E.G. Valerio, G. de M. Azevedo, Nucl. Instruments Methods Phys. Res. Sect. B Beam Interact. with Mater. Atoms 266 (2008) 2923–2927.

[36] T. Takeyama, T. Nakamura, N. Takahashi, M. Ohta, Solid State Sci. 6 (2004) 345–348.

[37] I. Omkaram, S. Buddhudu, Opt. Mater. (Amst). 32 (2009) 8–11.